The Astrophysical Journal, 630:1093–1106, 2005 September 10

THE EFFECT OF THE CORIOLIS FORCE ON KELVIN-HELMHOLTZ–DRIVEN MIXING IN PROTOPLANETARY DISKS

Gilberto C. Gómez and Eve C. Ostriker
Department of Astronomy, University of Maryland, College Park, MD 20742;
gomez@astro.umd.edu, ostriker@astro.umd.edu
Received 2005 February 4; accepted 2005 May 19

ABSTRACT

We study the stability of protoplanetary disks with vertical velocity gradients in their equilibrium rotation rates; such gradients are expected to develop when dust settles into the midplane. Using a linear stability analysis of a simple three-layer model, we show that the onset of instability occurs at a larger value of the Richardson number, and therefore for a thicker layer, when the effects of Coriolis forces are included. This analysis also shows that even-symmetry (midplane crossing) modes develop faster than odd-symmetry ones. These conclusions are corroborated by a large number of nonlinear numerical simulations with two different parameterized prescriptions for the initial (continuous) dust distributions. Based on these numerical experiments, the Richardson number required for marginal stability is more than an order of magnitude larger than the traditional $\frac{1}{4}$ value. The dominant modes that grow have horizontal wavelengths of several initial dust scale heights and in nonlinear stages mix solids fairly homogeneously over a comparable vertical range. We conclude that gravitational instability may be more difficult to achieve than previously thought and that the vertical distribution of matter within the dust layer is likely globally, rather than locally, determined.

Subject headings: hydrodynamics — instabilities — planets and satellites: formation — planetary systems: protoplanetary disks — turbulence

1. INTRODUCTION

In the generally accepted model for the formation of planets, the circumstellar disk—consisting of material remaining from the formation of the central star—progresses through a series of dynamical stages. Over the course of this evolution, the solids contained in the disk are believed to settle toward the midplane and form planetesimals, which in turn merge to assemble terrestrial planets and cores of gaseous giants. Unfortunately, some of the most basic elements of this model are not understood, with the detailed physical processes involved at many stages only barely explored.

One such poorly understood stage is the formation of planetesimals from interstellar dust.[1] It is generally accepted that micron-sized particles collide and stick together to form larger particles, but it is not clear that this stochastic coagulation process can continue up the ladder to generate kilometer-sized planetesimals. Among other difficulties with this model is the problem that bodies with approximate sizes between 1 cm and 1 m would drift radially inward very fast, as a consequence of drag with the partially pressure-supported gas disk in which they are embedded (Weidenschilling 1977). As a way of solving this problem, authors have looked for a process that allows particles to grow through this range of sizes in timescales similar to or smaller than the orbital time (Goldreich & Ward 1973; Weidenschilling 1980; Nakagawa et al. 1981, 1986; Weidenschilling & Cuzzi 1993). For example, Cuzzi et al. (1993) and Champney et al. (1995) noted that because particles of different sizes are affected differently by gas drag they would drift at different speeds, thus increasing their collision rate and possibly increasing the particle growth rate. Nevertheless, it remains questionable whether solid-state forces can grow particles through sticking, at the collision velocities likely present in protoplanetary disks (see discussion in Youdin & Shu 2002).

Gravitational instability (GI) has been proposed as an alternative (Safranov 1969; Goldreich & Ward 1973; Coradini et al. 1981; Sekiya 1983). In this model, as the dust settles vertically to create a dense midplane subdisk, the spatial particle density may increase until the layer crosses the GI density threshold. This model has the advantage that particle growth from millimeter to kilometer sizes happens on a short timescale. Still, there are uncertainties in this GI model. For example, several authors (Weidenschilling & Cuzzi 1993; Cuzzi et al. 1994; Weidenschilling 1995; Tanga et al. 2004) have pointed out that $\sim$10 m–sized bodies, an intermediate step of the two-stage process proposed by Goldreich & Ward (1973), reach the disk midplane with random velocities too large for GI to proceed.

A more frequently discussed problem with the GI hypothesis arises from the fact that as the solid particle density increases through vertical settling, the gas/dust mixture becomes less sensitive to large-scale gas pressure gradients that are likely to be present in the disk. With the loss of radially supporting pressure gradients, the dust-rich mixture near the midplane would orbit the central star with an orbital frequency closer to the Keplerian rate and thus develop a velocity shear with its dust-poor envelope. This velocity shear might trigger the Kelvin-Helmholtz instability (KHI), which could mix the dust and gas layers and stop particle settling before GI sets in (Goldreich & Ward 1973; Weidenschilling 1980). The question posed at this point is what are the appropriate circumstances for the development of the KHI in circumstellar disks? Or conversely, is it possible to have a KH-stable disk that is susceptible to GI and so able to form planetesimals within a very short timescale?

The most favorable circumstance for GI is if there is no turbulence—and no mixing of solids—in the absence of KHI. Sekiya & Ishitsu (2000, 2001) performed linear stability analyses of vertically shearing disks and concluded that GI can be

[1] In the outer parts of the disk, gaseous water, ammonia, and other molecules condense into ice, augmenting the dust with additional solids.

achieved, avoiding the KHI-induced mixing, only if the dust-to-gas surface density ratio is much larger than the solar abundance. Other authors have reached a similar conclusion while considering the potentially destabilizing influence of the Coriolis and tidal forces (Ishitsu & Sekiya 2002, 2003), stratification of the medium, two-fluid effects, and radiative cooling (Garaud & Lin 2004). Youdin & Shu (2002) further argued that the gas involved in the KHI should be able to drag and mix only a finite amount of solids, so that there might be a decoupling and precipitation of solids once the dust space density is large enough, even for particle sizes at which a good velocity coupling is expected. The precipitated particles would be free to continue settling and undergo GI. If a strong central enhancement of dust develops (Sekiya 1998) and precipitates out an independent solid layer, then potentially this reduces the needed dust-to-gas surface density enhancement required for planetesimals to form via GI. Even with the modification proposed by Youdin & Shu (2002), however, the dust-to-gas surface density ratio must be enhanced above solar abundance values, $\sim$0.01, by an order of magnitude.

Of course, this increased surface density ratio (which can also help accelerate stochastic coagulation) does not have to be global. Particle drift in the radial direction (Cuzzi et al. 1993; Youdin & Shu 2002; Haghighipour & Boss 2003; Weidenschilling 2003; Youdin & Chiang 2004) and self-gravitating spiral modes (Rice et al. 2004) could provide localized surface density concentrations of dust. Provided that these enhancements are long-lived, this could lead to localized GI.

As discussed above, when dust settles toward the midplane, both (destabilizing) shear and (stabilizing) buoyancy increase. In the situation in which dust and gas are coupled well enough, they may be considered a single fluid. For a stratified flow, competition between the opposing shear and buoyancy effects is traditionally described by the Richardson number,

$$\mathrm{Ri} = \frac{-gd\ln\rho/dz}{(dv/dz)^2}, \tag{1}$$

where $v(z)$ is the equilibrium shear velocity in the plane perpendicular to $\hat{\boldsymbol{e}}_z$. Miles (1961) and Howard (1961) proved (for incompressible flow in the Boussinesque approximation) that $\mathrm{Ri} < \frac{1}{4}$ somewhere in the layer is a necessary (but not sufficient) condition for instability (see also Drazin & Reid 1981, p. 325; a review of the proof is presented in Appendix B of Li et al. 2003). As Garaud & Lin (2004) argue, however, some of the assumptions in this proof, while acceptable in other physical regimes, are not applicable to the problem at hand.

In this paper, we explore the influence of an effect not considered in arriving at the "$\mathrm{Ri} > \frac{1}{4}$" stability criterion, namely the Coriolis force. In § 2 we present the basic equations of the model problem we have defined. In § 3 we perform a linear stability analysis of a discrete three-layer configuration, consisting of a dust-rich layer surrounded by dust-free gas. This analysis relaxes some of the assumptions made by previous work, compares modes of instability with even and odd symmetry, and assesses the effect of the Coriolis force. In § 4 we present the results of our numerical experiments, focusing on the effect the Coriolis force has on the stability of model disks with two different (continuous) initial dust distributions. Finally, in § 5 we present our conclusions.

2. BASIC EQUATIONS

Consider the reference frame of a fluid orbiting a central star at a distance R_0, with angular velocity $\boldsymbol{\Omega}_F$. For adiabatic flow of a gamma-law gas, the equations of hydrodynamics in this frame read

$$\frac{\partial\rho}{\partial t} + \nabla\cdot(\rho\boldsymbol{v}) = 0, \tag{2}$$

$$\frac{\partial\boldsymbol{v}}{\partial t} + (\boldsymbol{v}\cdot\nabla)\boldsymbol{v} = -\frac{\nabla P}{\rho} - \nabla\Phi - 2\boldsymbol{\Omega}_F\times\boldsymbol{v} - \boldsymbol{\Omega}_F\times(\boldsymbol{\Omega}_F\times\boldsymbol{R}), \tag{3}$$

$$\frac{\partial\mathcal{E}}{\partial t} + (\boldsymbol{v}\cdot\nabla)\mathcal{E} = -(P+\mathcal{E})\nabla\cdot\boldsymbol{v}, \tag{4}$$

$$P = (\gamma-1)\mathcal{E}. \tag{5}$$

All the symbols are standard. We orient the coordinate system with $\hat{\boldsymbol{e}}_z$ parallel to $\boldsymbol{\Omega}_F$, $\hat{\boldsymbol{e}}_x$ pointing radially, and $\hat{\boldsymbol{e}}_y$ pointing along the azimuthal background flow. We shall treat a small domain compared to R_0 and disregard the curvature terms in equations (2)–(5).

In addition to gas with density ρ_g, the flow contains a component of solids (dust + ice). We assume that the gas and solids are strongly coupled, so $\boldsymbol{v}_d = \boldsymbol{v}_g = \boldsymbol{v}$. In the strongly coupled limit, the dust component of the mixture adds inertia to the flow so that $\rho = \rho_g + \rho_d$ in equations (2) and (3), but the solids do not contribute to the pressure ($P = c_s^2\rho_g$, where c_s is the isothermal sound speed) and energy density in equations (4) and (5). The dust component also separately obeys a continuity equation,

$$\frac{\partial\rho_d}{\partial t} + \nabla\cdot(\rho_d\boldsymbol{v}) = 0. \tag{6}$$

For an axisymmetric equilibrium, the x- and z-components of the momentum equation read

$$\frac{v_{0y}^2(z)}{R_0} + 2\Omega_F v_{0y}(z) + \Omega_F^2 R_0 - \frac{\partial P_0/\partial R|_{R_0}}{\rho_d(z)+\rho_g(z)} - \Omega_{\mathrm{K}}^2 R_0 = 0, \tag{7}$$

$$-\frac{1}{\rho_d(z)+\rho_g(z)}\frac{\partial P_0}{\partial z} - \Omega_{\mathrm{K}}^2 z = 0. \tag{8}$$

Here, $\partial\Phi/\partial R \approx \Omega_{\mathrm{K}}^2 R$, where Ω_{K} is the Keplerian orbital frequency, and we approximate $\partial\Phi/\partial z \approx \Omega_{\mathrm{K}}^2 z$.

From equation (7), the orbital velocity of the flow in equilibrium depends on the dust abundance. In order to further specify our coordinate system, let us define Ω_F as the inertial frame orbital frequency of dust-free gas with a reference value of density at $z = 0$ of ρ_{g0}. With this definition of Ω_F, $v_{0y} = 0$ when $\rho_d = 0$, and we can relate Ω_F to the physical parameters of the system,

$$\frac{\Omega_F}{\Omega_{\mathrm{K}}} = \left(1 + \frac{\partial P_0/\partial R|_{R_0,z=0}}{\Omega_{\mathrm{K}}^2 R_0\rho_{g0}}\right)^{1/2}. \tag{9}$$

Here, P_0 is the pressure in the dust-free case.

Solving equation (7) for v_{0y} and taking $|v_{0y}| \ll \Omega_F R_0$, we obtain

$$v_{0y} = v_{0,\max}\left(\frac{\mu}{1+\mu}\right), \tag{10}$$

where $\mu(z) = \rho_d(z)/\rho_g(z)$ is the dust abundance and

$$v_{0,\max} = -\frac{\partial P_0/\partial R|_{R_0,z=0}}{2\Omega_F\rho_{g0}} \tag{11}$$

is the maximum speed that the dust-laden gas can attain, i.e., the difference between the Keplerian velocity and $\Omega_F R_0$.[2]

In order to define $P_0(R)$ we adopt the parametrization of Youdin & Shu (2002),

$$\Sigma_g(R) = 1700 \text{ g cm}^{-2} f_g \left(\frac{R}{1 \text{ AU}}\right)^{-p}, \quad (12)$$

$$T(R) = 280 \text{ K } f_T \left(\frac{R}{1 \text{ AU}}\right)^{-q}, \quad (13)$$

where Σ_g is the gas surface density and T is the temperature of the gas. For the minimum solar nebula (MSN) model of Hayashi (1981), $f_g = f_T = 1$, $p = 3/2$, and $q = \frac{1}{2}$. In this case, $v_{0,\max}/c_s$ depends only weakly on R,

$$\frac{v_{0,\max}}{c_s} = 7.3 \times 10^{-2} \left(\frac{R}{1 \text{ AU}}\right)^{1/4}. \quad (14)$$

Consider now the vertical hydrostatic equilibrium. For vertically isothermal conditions, equation (8) can be written as

$$\frac{\partial \ln \rho_g}{\partial z} = -\frac{\Omega_K^2 z}{c_s^2}[1 + \mu(z)], \quad (15)$$

which can be solved (analytically or numerically) for $\rho_g(z)$, given $\mu(z)$. The total density is then $\rho = \rho_g(1 + \mu)$. In § 4 we define initial conditions either by setting $\mu(z)$ to a specified function or by requiring the solution $\mu(z)$ to satisfy certain additional assumptions.

In describing the equilibrium, we have introduced a natural set of units, namely $1/\Omega_K$ for time, c_s for velocity, and ρ_{g0} for density. For future reference, we note that in the dust-free case, the solution of equation (15) is a Gaussian with gas column density $\Sigma_g = (2\pi)^{1/2}\rho_{g0}H_g$, where $H_g = c_s/\Omega_K$. In the MSN model, the gas disk aspect ratio is

$$\frac{H_g}{R} = 4.5 \times 10^{-2} \left(\frac{R}{1 \text{ AU}}\right)^{1/4}. \quad (16)$$

3. STABILITY ANALYSIS FOR A THREE-LAYER MODEL

3.1. *Perturbation Equations and General Solution*

Consider a perturbation to the above equilibrium with $\rho = \rho_0 + \rho_1$, $\boldsymbol{v} = \boldsymbol{v}_0 + \boldsymbol{v}_1$, and $P = P_0 + P_1$. We assume that the flow is incompressible ($\nabla \cdot \boldsymbol{v}_1 = 0$), linearize equations (2)–(5), and for simplicity in this first study, drop terms in $\partial/\partial x$. Then, taking ρ_1, P_1, v_{1x}, v_{1y}, and $v_{1z} \propto \exp[i(k_y y - \omega t)]$, the resulting equations can be combined to obtain a governing equation for v_{1z}:

$$\left[1 - \frac{4\Omega_F^2}{(\omega - k_y v_{0y})^2}\right]\partial_z^2 v_{1z} + \left\{\partial_z \ln \rho_0 \left[1 - \frac{4\Omega_F^2}{(\omega - k_y v_{0y})^2}\right] - \frac{4\Omega_F^2 k_y}{(\omega - k_y v_{0y})^3}\partial_z v_{0y}\right\}\partial_z v_{1z} + \left[\frac{k_y}{\omega - k_y v_{0y}}\partial_z \ln \rho_0 \partial_z v_{0y} + \frac{k_y}{\omega - k_y v_{0y}}\partial_z^2 v_{0y} - k_y^2 - \frac{k_y^2 g(z)\partial_z \ln \rho_0}{(\omega - k_y v_{0y})^2}\right] v_{1z} = 0, \quad (17)$$

where $\partial_z = \partial/\partial z$.

[2] The expression $v_{0,\max}$ relates to the η_K parameter used in previous work by $v_{0,\max} = \eta_K R_0 \Omega_K^2/\Omega_F$.

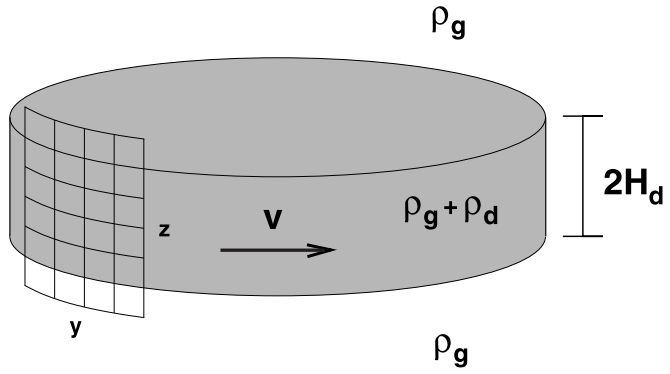

FIG. 1.—Schematic of the discrete three-layer model. A central gas-dust layer, with density $\rho_g + \rho_d$ and thickness $2H_d$, is sandwiched between two semi-infinite gaseous atmosphere layers with densities ρ_g. In the reference frame rotating with the atmosphere at Ω_F, the central layer has velocity V at radius R_0. We consider a small azimuthal vertical section of the disk, as shown.

The usual step at this point is to invoke the Boussinesque approximation, dropping $\partial_z \rho_0$ everywhere but in the buoyancy term. Because shear and density gradients are directly associated for the problem at hand, however, we shall not make this approximation in this work (see also discussion in Garaud & Lin 2004).

Consider now the three-layer distribution shown in Figure 1. The middle layer is composed of the dust and gas mixture, while the top and bottom layers are dust-free. We take the initial dust density ρ_d as constant in the middle layer and the gas density ρ_g constant across all layers (provided H_d is small compared to the total disk thickness H_g, the latter is true more generally). This three-layer model is a fair approximation to a more realistic continuous distribution for wavelengths larger than the vertical velocity and density gradient scales.

In the chosen reference frame, the top and bottom layers are at rest, while the central layer has a constant velocity $V = v_{0,\max}\rho_d/(\rho_g + \rho_d) = v_{0,\max}\mu/(1 + \mu)$. Since $\partial_z \rho_0 = \partial_z v_{0y} = 0$ within each layer, equation (17) simplifies to

$$\partial_z^2 v_{1z} = \begin{cases} \dfrac{k_y^2}{1 - 4\Omega_F^2/\omega^2} v_{1z}, & |z| > H_d, \\ \dfrac{k_y^2}{1 - 4\Omega_F^2/(\omega - k_y V)^2} v_{1z}, & |z| < H_d. \end{cases} \quad (18)$$

The solution is

$$v_{1z} = \begin{cases} A_1 e^{-K_1 z}, & z > H_d, \\ A_{2+} e^{K_2 z} + A_{2-} e^{-K_2 z}, & |z| < H_d, \\ A_3 e^{K_1 z}, & z < -H_d, \end{cases} \quad (19)$$

where

$$K_1 = \frac{k_y}{\sqrt{1 - 4\Omega_F^2/\omega^2}}, \quad (20)$$

$$K_2 = \frac{k_y}{\sqrt{1 - 4\Omega_F^2/(\omega - k_y V)^2}}, \quad (21)$$

and where we require that the sign of the square root in equation (20) is to be chosen such that its real part $\Re(K_1) > 0$. In order to obtain equation (19), we apply the boundary condition

$v_{1z} \rightarrow 0$ when $|z| \rightarrow \infty$. In general, solutions that are either midplane symmetric or midplane antisymmetric are possible. Some previous work (Ishitsu & Sekiya [2002], for example) has explored only the case in which v_{1z} is an odd function of z, so $v_{1z}(0) = 0$. We shall focus much of our attention on the case in which v_{1z} is an even function and explore the odd case only for reference.

3.2. *Solutions with v_{1z} Even in z*

In the case with $v_{1z}(z) = v_{1z}(-z)$, $A_1 = A_3$ and $A_{2+} = A_{2-} = A_2$. To relate A_1 and A_2, we use the fact that the vertical displacement of a Lagrangian point, $\delta z = iv_{1z}/(\omega - k_y V)$, must be a continuous function of z across any interface in the flow. Applying this condition at the layer discontinuity, this implies

$$e^{-K_1 H_d} A_1 = \frac{\omega}{\omega - k_y V} A_2 (e^{K_2 H_d} + e^{-K_2 H_d}). \tag{22}$$

By integrating equation (17) across the $z = H_d$ interface and substituting the solutions (19), we obtain the dispersion relation,

$$(1+\mu)(\omega - k_y V)^2 \left[1 - \frac{4\Omega_F^2}{(\omega - k_y V)^2}\right]^{1/2} \times \tanh(K_2 H_d) + \omega^2 \left(1 - \frac{4\Omega_F^2}{\omega^2}\right)^{1/2} = k_y g \mu. \tag{23}$$

Here, $g = g(H_d) = \Omega_K^2 H_d$.

If we temporarily disregard the Coriolis terms (setting $\Omega_F = 0$; we discuss the case with $\Omega_F \neq 0$ in § 3.5), then $K_1 = K_2 = k_y$, and we can analytically solve equation (23) for ω. The condition for instability [that the imaginary part of ω, $\Im(\omega)$, is nonzero] is

$$k_y V^2 > \frac{g\mu}{1+\mu} \left[\frac{1}{\tanh(k_y H_d)} + 1 + \mu\right] \tag{24}$$

(see also Drazin & Reid 1981, p. 29). This can be written in an alternate form as

$$k_y H_d > \frac{1+\mu}{\mu} \left(\frac{H_d}{H_g}\right)^2 \left(\frac{c_s}{v_{0,\max}}\right)^2 \left[\frac{1}{\tanh(k_y H_d)} + 1 + \mu\right]. \tag{25}$$

We now define an effective Richardson number for the discontinuous distribution in the three-layer model,

$$\begin{aligned} \mathrm{Ri}_{\mathrm{eff}} &\equiv \frac{-g(\Delta\rho/\Delta z)}{\rho(V/\Delta z)^2} \\ &= \frac{1+\mu}{\mu} \left(\frac{H_d}{H_g}\right)^2 \left(\frac{c_s}{v_{0,\max}}\right)^2 \\ &= \frac{\pi}{2} \frac{1+\mu}{\mu^3} \left(\frac{\Sigma_d}{\Sigma_g}\right)^2 \left(\frac{c_s}{v_{0,\max}}\right)^2, \end{aligned} \tag{26}$$

where $\Sigma_d = 2\rho_d H_d$ is the dust column density, so that

$$\mu = \sqrt{\frac{\pi}{2}} \frac{H_g}{H_d} \frac{\Sigma_d}{\Sigma_g}. \tag{27}$$

With this definition, the criterion for instability may be written

$$\mathrm{Ri}_{\mathrm{eff}} < \frac{k_y H_d \tanh(k_y H_d)}{1 + (1+\mu)\tanh(k_y H_d)}. \tag{28}$$

Note that for $\mu \gg 1$ and a moderate $k_y H_d$ value, equation (28) reduces to $\mathrm{Ri}_{\mathrm{eff}} < (k_y H_d)/\mu$, i.e., the layer will still remain stable to wavelengths comparable to H_d even when $\mathrm{Ri}_{\mathrm{eff}}$ is quite small, for a sufficient dust concentration.

3.3. *Solutions with v_{1z} Odd in z*

In the case with $v_{1z}(z) = -v_{1z}(-z)$, $A_1 = -A_3$, and $A_{2+} = -A_{2-} = A_2$, equation (22) becomes

$$e^{-K_1 H_d} A_1 = \frac{\omega}{\omega - k_y V} A_2 (e^{K_2 H_d} - e^{-K_2 H_d}). \tag{29}$$

The resulting dispersion relation for the odd-symmetry mode is

$$(1+\mu)(\omega - k_y V)^2 \left[1 - \frac{4\Omega_F^2}{(\omega - k_y V)^2}\right]^{1/2} \times \coth(K_2 H_d) + \omega^2 \left(1 - \frac{4\Omega_F^2}{\omega^2}\right)^{1/2} = k_y g \mu. \tag{30}$$

Again, if we consider the $\Omega_F = 0$ case, we can obtain criteria for instability. These are the same as equations (24), (25), and (28), with $\coth(k_y H_d)$ substituted for $\tanh(k_y H_d)$. Notice that both the even and odd modes have the same instability condition for short wavelengths ($k_y H_d \gg 1$),

$$\mathrm{Ri}_{\mathrm{eff}}(2+\mu) < k_y H_d \quad \text{or} \quad \frac{g\mu(2+\mu)}{1+\mu} < k_y V^2, \tag{31}$$

which is the same as the standard criterion (Chandrasekhar 1981, eq. [XI.34], for example) for KHI at an interface between two semi-infinite layers.

3.4. *Comparing Even and Odd Modes With $\Omega_F = 0$.*

In order to compare with more realistic models that have a continuous distribution of dust, we focus on wavelengths that are comparable to the layer thickness; shorter wavelengths will not lead to large-scale mixing of the dust layer, and longer wavelengths have smaller growth rates. Figure 2 shows the minimum stable layer thickness for three different values of $k_y H_d$ for a range of dust-to-gas surface density ratios and $v_{0,\max}/c_s = 0.1$. Both even- and odd-symmetry solutions are shown. In a real system, the dust will (at least initially) likely settle toward the midplane at a higher rate than the surface density ratio changes. So we can imagine the disk evolving down along a vertical line in Figure 2, until it reaches the stability edge at a relevant wavelength. On a longer timescale, the disk may then move along that edge toward larger Σ_d/Σ_g values as gas is lost to photoevaporation or the dust component is increased due to radial drift, for example.

The slopes of the critical curves at fixed $k_y H_d$ can be understood physically. At small Σ_d/Σ_g, an increase in Σ_d/Σ_g increases μ, thus increasing the velocity shear, since $V = v_{0,\max}\mu/(1+\mu)$. This forces an increase in H_d/H_g in order to keep the layer marginally stable; as a consequence, from equation (25) the critical $(H_d/H_g) \propto (\Sigma_d/\Sigma_g)^{1/3}$ at small μ. For large Σ_d/Σ_g, $\mu \gg 1$, and the velocity difference saturates to $v_{0,\max}$; in this case, the dust layer must get thinner to remain marginally stable with increasing dust abundance. At large μ, the critical curve therefore follows

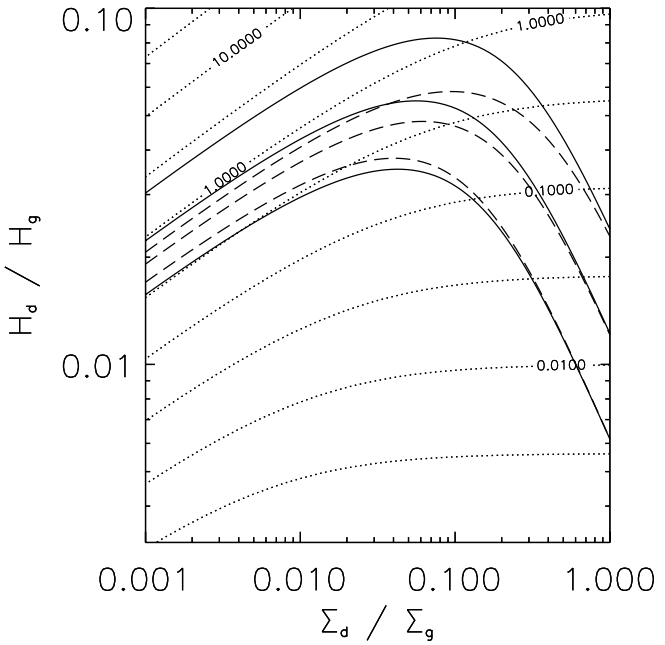

FIG. 2.—Minimum stable dust layer thickness for global modes with $\Omega_F = 0$ (i.e., neglecting Coriolis forces), as a function of the dust-to-gas surface density ratio. Both even (*solid lines*) and odd modes (*dashed lines*) are shown for fixed values of $k_y H_d = \pi, \pi/2$, and $\pi/4$ (*top, middle, and bottom, respectively*). Curves of constant effective Richardson number (*dotted lines*) are overlaid. $\mathrm{Ri}_{\mathrm{eff}} =$ constant is a good stability proxy at low Σ_d/Σ_g.

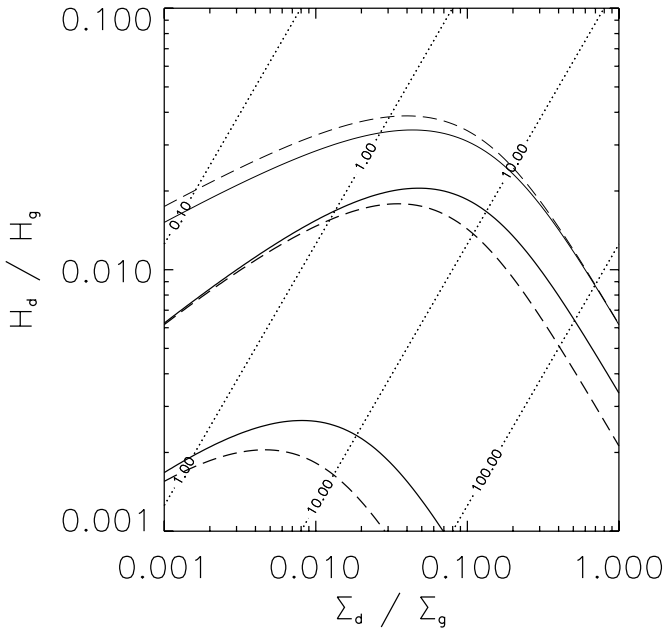

FIG. 3.—Instability growth rates for $k_y H_d = \pi/4$ and $\Omega_F = 0$. Lines show the even (*solid lines*) and odd (*dashed lines*) modes for values of the growth rate (*from the top down*) $\omega_I/\Omega_{\mathrm{K}} = 0$ (stability edge), 1, and 10. Dotted lines follow $\mu =$ constant.

$(H_d/H_g) \propto (\Sigma_d/\Sigma_g)^{-1}$. These small- and large-μ scalings of $(H_d/H_g)_{\mathrm{crit}}$ with Σ_d/Σ_g are the same as those that have been identified by Garaud & Lin (2004) in their equations (C3) and (C9), respectively.

Lines of constant $\mathrm{Ri}_{\mathrm{eff}}$ are also plotted in Figure 2. Recall that for a continuous dust distribution, $\mathrm{Ri} < \frac{1}{4}$ is a necessary (but not sufficient) condition for the development of the KHI. For our discrete three-layer distribution, $\mathrm{Ri}_{\mathrm{eff}} =$ constant is a good proxy for the stability limit of both even and odd modes at fixed $k_y H_d$, but only at low Σ_d/Σ_g. For $k_y H_d = \pi/4$, we find that the critical $\mathrm{Ri}_{\mathrm{eff}} \approx 0.3$ at $\Sigma_d/\Sigma_g \lesssim 0.01$, close to the $\mathrm{Ri} = \frac{1}{4}$ result of Miles (1961) and Howard (1961). At larger Σ_d/Σ_g, the layer is too heavy to be easily disturbed by a global mode. In this case, with $\mu \gg 1$, the stability limit (for either even- or odd-symmetry modes) is $\mathrm{Ri}_{\mathrm{eff}} = k_y H_d/\mu$. So, at given $\mathrm{Ri}_{\mathrm{eff}}$ and H_d/H_g, the increasingly short wavelengths that are required for instability with increasing Σ_d/Σ_g would make the disturbance only a surface phenomenon. Global instabilities only become possible when H_d/H_g, and hence $\mathrm{Ri}_{\mathrm{eff}}$ decreases. Garaud & Lin (2004) find, similarly, that the critical value of Ri decreases as Σ_d/Σ_g increases above ≈ 0.01 for the value of $v_{0,\max}/c_s$ we adopt.

For large Σ_d/Σ_g and fixed $k_y H_d$, Figure 2 shows that the maximum unstable H_d/H_g has the same wavelength for both the even and odd modes. But the growth rates are not the same, as shown in Figure 3. As the layer thickness decreases at constant surface density, even modes at a given $k_y H_d$ will develop more rapidly than the corresponding odd modes. Or conversely, an even mode with a longer wavelength (and more efficient dilution of the dust layer) will become excited at the same time as a (less efficient) odd mode with a shorter wavelength. This can be expected, since the incompressibility condition implies, for the odd mode, that a horizontal converging flow must be generated in the midplane at the position where the interface displacement makes the layer thicker ($\delta z/z > 0$). Since the even mode does not need to channel energy into this requirement, it can grow faster. On the other hand, since the odd mode does not need to vertically displace the whole layer, it can remain unstable for larger H_d/H_g values, for which gravity is stronger at the layer interface.

3.5. *Even Mode, Including Coriolis Forces* ($\Omega_F \neq 0$)

In §§ 3.2 and 3.3 we studied the solutions of equations (23) and (30) obtained when the Coriolis forces are neglected. While the solutions presented were for the exact equations, we have found that taking the long-wavelength limit $k_y H_d \ll 1$ yields a good approximation to the stability even at relatively large values of $k_y H_d$ ($\sim$10). When the Coriolis terms are included ($\Omega_F \neq 0$), the dispersion relation retains its simple character when $k_y H_d \ll 1$, so for this section we concentrate on that limit.[3]

In the long-wavelength regime, equation (23) can be written as

$$(1+\mu)(\omega - k_y V)^2 k_y H_d + \omega^2 \left(1 - \frac{4\Omega_F^2}{\omega^2}\right)^{1/2} = k_y g \mu, \quad (32)$$

where we require the real part of the square root to be positive. The procedure used to solve equation (32) is presented in the Appendix, and the corresponding roots are shown in Figure 4. The number and nature of the roots can change only at critical H_d/H_g values (as described in the Appendix), marked in Figure 4 by the vertical lines.

For the parameters presented in Figure 4*b*, there is a range of values of H_d/H_g with only real solutions, which implies stability. Nevertheless, we consider the existence of this gap of limited practical significance since the gap closes for longer wavelengths (which yield more efficient vertical mixing). More significant is the fact that there are no solutions, real or complex, when $(k_y V/\Omega_{\mathrm{K}})^2 < \mu/(1+\mu)$ or $k_y v_{0,\max}/\Omega_{\mathrm{K}} < (1+1/\mu)^{1/2}$ (right-hand side of Fig. 4). The transition critical point corresponds to $\omega/\Omega_{\mathrm{K}} = 0$.

[3] For short wavelengths, $k_y H_d \gg 1 \Rightarrow \tanh(K_2 H_d) \approx 1$, and eq. (23) yields the same dispersion relation as the two-layer problem with rotation studied by Chandrasekhar (1981, § 105); see also Huppert (1968).

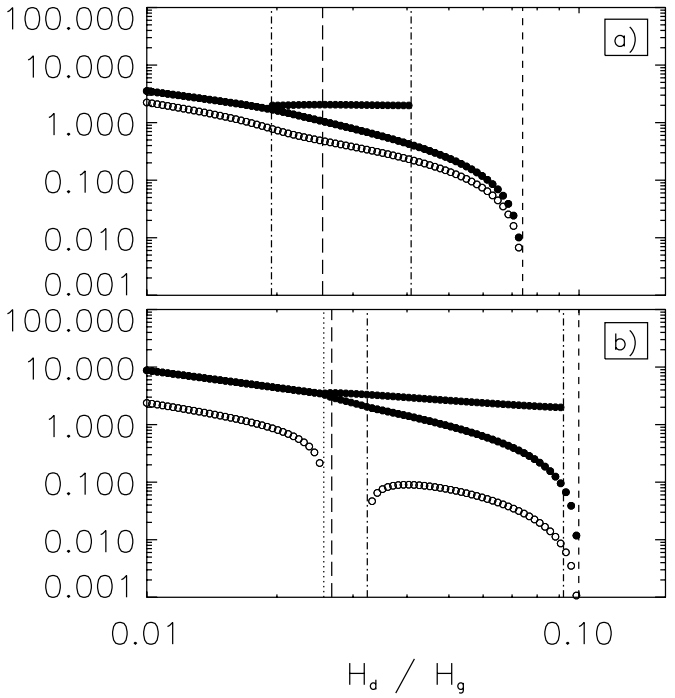

FIG. 4.—Roots of eq. (32), as a function of H_d/H_g, for $k_y H_d = \pi/3$ with (*a*) $\mu = 1$ and (*b*) $\mu = 10$. Filled circles show $\Re(\omega)$, and open circles show $\Im(\omega)$. Vertical lines mark critical H_d/H_g values (see Appendix). There is no solution for $\mathrm{Ri}_{\mathrm{eff}} > (k_y H_d)^2$, i.e., large H_d/H_g.

For given (order unity) $k_y H_d$ and any Σ_d/Σ_g, sufficiently small μ guarantees that this condition holds. Thus, using equation (26), a necessary (but not sufficient) condition for instability at long wavelengths appears to be

$$\mathrm{Ri}_{\mathrm{eff}} < (k_y H_d)^2. \tag{33}$$

Comparison of equation (33) and its equivalent for the $\Omega_F = 0$ case (eq. [28]) shows that a larger $\mathrm{Ri}_{\mathrm{eff}}$ is required for stability when the Coriolis terms are turned on: for $k_y H_d = \pi/3$, the critical value for $\mathrm{Ri}_{\mathrm{eff}}$ is 1.1 when $\Omega_F \neq 0$, compared to 0.32, 0.14, and 0.09 for $\mu = 1$, 5, and 10, respectively, when $\Omega_F = 0$. Notice that both conditions reduce to the same criterion for instability when $k_y H_d$ and $\mu \ll 1$. However, small μ and $\mathrm{Ri}_{\mathrm{eff}} < (k_y H_d)^2 < 1$ are satisfied only for $\Sigma_d/\Sigma_g \ll 0.01$, i.e., for cases with much lower metallicity than that expected in the protosolar nebula.

An interesting feature of equation (33) is that (unlike eq. [28]) it does not explicitly depend on the dust abundance, μ. This is due to the fact that at the onset of instability for the $\Omega_F \neq 0$ case, the phase velocity vanishes [$\Re(\omega) \rightarrow 0$]. This has two consequences. First, a larger fraction of the heavier layer's momentum is available to help destabilize the flow (and so, the layer remains unstable for larger $\mathrm{Ri}_{\mathrm{eff}}$). Second, a vanishingly small ω means a small K_1 (eq. [20]), so that vertical pressure gradients in the gas layers are very small. So, as the dust/gas mixture flows through the sinuous locus of the perturbed midplane layer, only the centrifugal force in the vertical direction ($V^2 k_y^2 \delta z$) and gravity ($\Omega_{\mathrm{K}}^2 \delta z$) are involved in force balancing, while gas pressure gradients are negligible. In contrast, for the $\Omega_F = 0$ case, $\Re(\omega)$ is nonvanishing at the onset of instability, yielding a finite K_1 value. This implies nonnegligible vertical pressure gradients, which introduce a dependence on the dust-to-gas density ratio in the force balance. Small or vanishing $\Re(\omega)$ is possible only in the $\Omega_F \neq 0$ case, when the Coriolis forces (from v_{1x}) are able to partly, or fully, compensate azimuthal pressure forces.

We can alternatively write the instability condition for $\Omega_F \neq 0$ in terms of more basic physical parameters by considering equation (26) in the large- and small-μ limits:

$$\frac{H_d}{H_g} < \begin{cases} \left(\dfrac{\pi}{2}\right)^{1/6} \left(\dfrac{\Sigma_d}{\Sigma_g}\right)^{1/3} \left(\dfrac{v_{0,\max}}{c_s}\right)^{2/3} (k_y H_d)^{2/3}, & \mu \ll 1, \\ \dfrac{v_{0,\max}}{c_s} k_y H_d, & \mu \gg 1. \end{cases} \tag{34}$$

Note that the minimum stable layer thickness approaches a constant value as Σ_d/Σ_g increases, as shown by the dotted lines of Figure 2. This stands in contrast with the instability criterion for the $\Omega_F = 0$ case (see eq. [25] and Fig. 2), for which $(H_d/H_g)_{\mathrm{crit}} \propto (\Sigma_d/\Sigma_g)^{-1}$ as the surface density increases. Thus, for large μ, the instability criterion is $\Omega_{\mathrm{K}} < v_{0,\max} k_y$ for $\Omega_F \neq 0$, compared to $(\mu k_y H_d)^{1/2} \Omega_{\mathrm{K}} < v_{0,\max} k_y$ for $\Omega_F = 0$.

While we have concentrated on the long-wavelength limit in the discussion of this section, we note that the general dispersion relation of equation (23) can easily be solved in the limit $|\omega| \rightarrow 0$. When $\Omega_F \neq 0$, an unstable solution will appear when $\mathrm{Ri}_{\mathrm{eff}}$ passes below the value

$$\mathrm{Ri}_{\mathrm{crit}} = (k_y H_d)^2 \tanh\left[\frac{k_y H_d}{\sqrt{1 - 4\Omega_F^2/(k_y V)^2}}\right] \frac{\sqrt{1 - 4\Omega_F^2/(k_y V)^2}}{k_y H_d}, \tag{35}$$

with growth rate $\propto(\mathrm{Ri}_{\mathrm{crit}} - \mathrm{Ri}_{\mathrm{eff}})\Omega_F$. Thus, the necessary criterion for instability in the long-wavelength limit is quite similar to a more general *necessary and sufficient* criterion for a marginally unstable mode to appear. Since $\tanh(\chi)/\chi > 1$, $\mathrm{Ri}_{\mathrm{crit}}$ is in practice slightly larger than the value deduced in the long-wavelength limit.

We note that for the odd-symmetry case, the critical $\mathrm{Ri}_{\mathrm{eff}}$ is given by the same expression as above, with $\coth(x)$ substituted for $\tanh(x)$; for long wavelengths, the instability criterion is therefore $(k_y V)^2 > 4\Omega_F^2 + k_y^2 g H_d \mu/(1+\mu)$, or using $\Omega_F \approx \Omega_{\mathrm{K}}$,

$$\mathrm{Ri}_{\mathrm{eff}} < \frac{(k_y H_d)^2 \mu}{4(1+\mu) + (k_y H_d)^2 \mu}. \tag{36}$$

This is always smaller than the criterion for the even-symmetry case, and $\mathrm{Ri}_{\mathrm{crit}} \rightarrow (k_y H_d)^2/[4 + (k_y H_d)^2]$ for $\mu \gg 1$.

Finally, we note that the conclusions based on the odd-symmetry three-layer system are similar to those for the two-layer system considered by Chandrasekhar (1981). For the two-layer system with rotation, instability first becomes possible when

$$(k_y V)^2 > 2\Omega_F^2 + \left[4\Omega_F^4 + k_y^2 g^2 \left(\frac{\mu}{1+\mu}\right)^2\right]^{1/2}. \tag{37}$$

This can also be written, taking $\Omega_F \approx \Omega_{\mathrm{K}}$, as

$$\mathrm{Ri}_{\mathrm{eff}} < \frac{(k_y H_d)^2 \mu}{2(1+\mu) + \sqrt{4(1+\mu)^2 + (k_y H_d)^2 \mu^2}}. \tag{38}$$

For $\mu \gg 1$, this yields $\mathrm{Ri}_{\mathrm{crit}} = (k_y H_d)^2/\{2 + [4 + (k_y H_d)]^{1/2}\}$, very similar to the odd-symmetry three-layer case.

4. NUMERICAL SIMULATIONS

4.1. *Basic Numerical Methods*

With our physical understanding developed via the instability analysis of the simple three-layer model in § 3, we now turn to fully nonlinear simulations with a continuous dust distribution. Our solutions of equations (2)–(5) are obtained using a version of ZEUS (Stone & Norman 1992), a finite-difference, time-explicit, operator-split, Eulerian code for numerical hydrodynamics. For the purpose of this investigation, we implemented source terms corresponding to the Coriolis force and the background radial pressure gradient. We treat this background radial pressure gradient as constant in time and space, $-\partial P_0/\partial R \equiv 2\Omega_F \rho_{g0} v_{0,\max}$.

As described in § 2, in the strong-coupling limit both the gas and dust separately obey the continuity equation (eqs. [2] and [6]). We implement this requirement in ZEUS by updating ρ_d using the same transport algorithm as used for the total density, $\rho = \rho_g + \rho_d$. We have tested this implementation by advecting a one-dimensional, Gaussian-shaped "dust cloud" in pressure equilibrium with its surroundings. A constant velocity was given to the full grid (200 zones), which advected the dust along five cloud lengths and across the periodic boundaries. This experiment was repeated for each coordinate direction of the code. In all cases, the total dust mass remained constant, and the rms deviation from the initial Gaussian shape was only 0.4%.

Since ZEUS was not designed to solve incompressible flow problems, we need to verify that its algorithms yield acceptable solutions in the regime of interest and, in particular, can properly evolve KHIs. To test this, we simulated a velocity shear slab with a discrete jump in velocity and density, similar to the setup in § 3, with the Coriolis terms turned off. These simulations were performed in a two-dimensional y-z plane with initial velocity $\boldsymbol{v} = v_y(z)\hat{\boldsymbol{e}}_y$. The initial conditions were perturbed with an eigenfunction of the even mode, having a specified wavelength. We then measured the growth rate of the specified perturbed mode while it remained in the linear phase and before other modes (faster growing with smaller wavelengths, seeded by grid-size noise) interfered in any obvious way. We compared this growth rate with the analytical value for a variety of perturbation amplitudes, obtaining an agreement of the order of 10%.

We now move on to the initialization of our full nonlinear, continuous simulations. For each model, we set up a disk atmosphere in vertical hydrostatic equilibrium and with azimuthal velocity $v_y(z)$ compensating radial gravity and the background pressure gradient. As described in § 2, setting the value of $\mu(z) = \rho_d(z)/\rho_g(z)$ defines all the hydrodynamic variables in the equilibrium state.

4.2. *Experiments with Prescribed $\mu(z)$*

The experiments described in this section are initialized by simply defining μ as an arbitrary function of z, namely,

$$\mu(z) = \mu_0 \mathrm{sech}^2(z/H_d), \tag{39}$$

with $\mu_0 = \mu(0)$. Three parameters uniquely define a model: μ_0, $v_{0,\max}/c_s$, and H_d/H_g. (For consistency with § 3, in practice we shall use Σ_d/Σ_g instead of μ_0.) In these experiments, the simulation domain is a square grid of size $20H_d$ (257×257 grid points), with periodic x- and y-boundaries and closed z-boundaries.[4]

[4] We also tested open z-boundaries and found no significant differences.

The equilibrium state is perturbed by random velocities with a maximum amplitude of $10^{-3}c_s$. In all cases, $v_{0,\max} = 0.1c_s$, which for MSN parameters, corresponds to a radial location at $R \approx 3.5$ AU.

Figure 5 shows results from the simulations with $H_d = 0.01H_g$ and $\Sigma_d = 0.008\Sigma_g$, both with the Coriolis terms turned off (*left*; $\Omega_F = 0$) and with the Coriolis terms turned on (*right*; $\Omega_F \neq 0$). The density snapshots presented are $t = (1.5, 2.2, 2.9)t_{\mathrm{orb}}$ ($\Omega_F = 0$), and $t = (1.8, 2.3, 2.8)t_{\mathrm{orb}}$ ($\Omega_F \neq 0$), where $t_{\mathrm{orb}} = 2\pi/\Omega_{\mathrm{K}}$ is the orbital time. The initial linear growth phase is very similar for both cases, with a sinusoidal displacement of the dust layer consistent with the even (midplane crossing) mode of the instability. Notice that the instability develops three wavelengths in the computation domain, which corresponds to $k_y H_d \approx 0.95$. We also performed simulations with 3 and 5 times larger grids in the y-direction (at lower resolution) and found that the same approximate $k_y H_d$ mode predominated. The fastest growing mode in the analysis presented in Ishitsu & Sekiya (2002, 2003) has a similar $k_y H_d$ value.

In the $\Omega_F = 0$ case, once the displacement is large enough, drag with the dust-poor fluid erodes the tips of the displaced layer, generating familiar backward-facing KH rolls. The flow around the rolls pushes the dust toward the peaks, where it accumulates until the layer breaks. After the wave breaks, the dust mixes with the surrounding gas, lowering the dust abundance and the velocity shear and generating a more-or-less homogeneous layer with a thickness similar to the wavelength of the linear growth. (For some parameter choices, this layer is in turn unstable and again develops a linear growth phase.) Remnant nonorganized motions generate diffusion that further increases the layer thickness over longer timescales.

In contrast to the $\Omega_F = 0$ model, after the linear growth phase the $\Omega_F \neq 0$ case has a period of very rapid evolution. Unlike the $\Omega_F = 0$ case, the dust accumulates in the midplane at the nodes of the displaced layer. As the vertical displacement grows, the leading faces of the perturbed dust layer encounter the slower moving high-latitude gas. As the gas is pushed by the dust, it gains angular momentum and flows radially outward (see Fig. 6). Correspondingly, the dusty layer loses angular momentum and flows radially inward, increasing its azimuthal velocity. As a consequence, the displaced peaks move faster than the gas in the midplane, generating forward-leaning structures. When the initial density layer loses integrity, it forms a new layer thicker than that generated in the $\Omega_F = 0$ case. The subsequent diffusive growth also develops more rapidly.

Nearly every set of parameters we tested triggered growth dominated by an even mode, consistent with expectations from the discussion in § 3.4. In order to induce the development of the odd mode, we forced the vertical symmetry by placing a boundary of the simulation at $z = 0$, for the $\Omega_F = 0$ case, at the same spatial resolution. Results for this experiment are shown in Figure 7. (The grid is doubled in this plot for easier comparison with Fig. 5.) There are several differences evident between these examples of even and odd modes. First, the odd mode develops longer wavelengths, fitting only two wavelengths in the domain, evolving later to a single wavelength. Second, despite the longer wavelength, the extent of the layer after the nonlinear growth phase is thinner, with the dust accumulated at the midplane. Third, this (and other) odd-mode simulations evolve much more slowly than the even-mode ones. This odd-mode simulation has a much larger latency time, despite the fact that the initial perturbations are a factor of 10 larger than the even-mode example. The dominant wavelengths that develop for the even modes have larger growth rates than those for the odd modes: for this case, $0.58\Omega_{\mathrm{K}}$

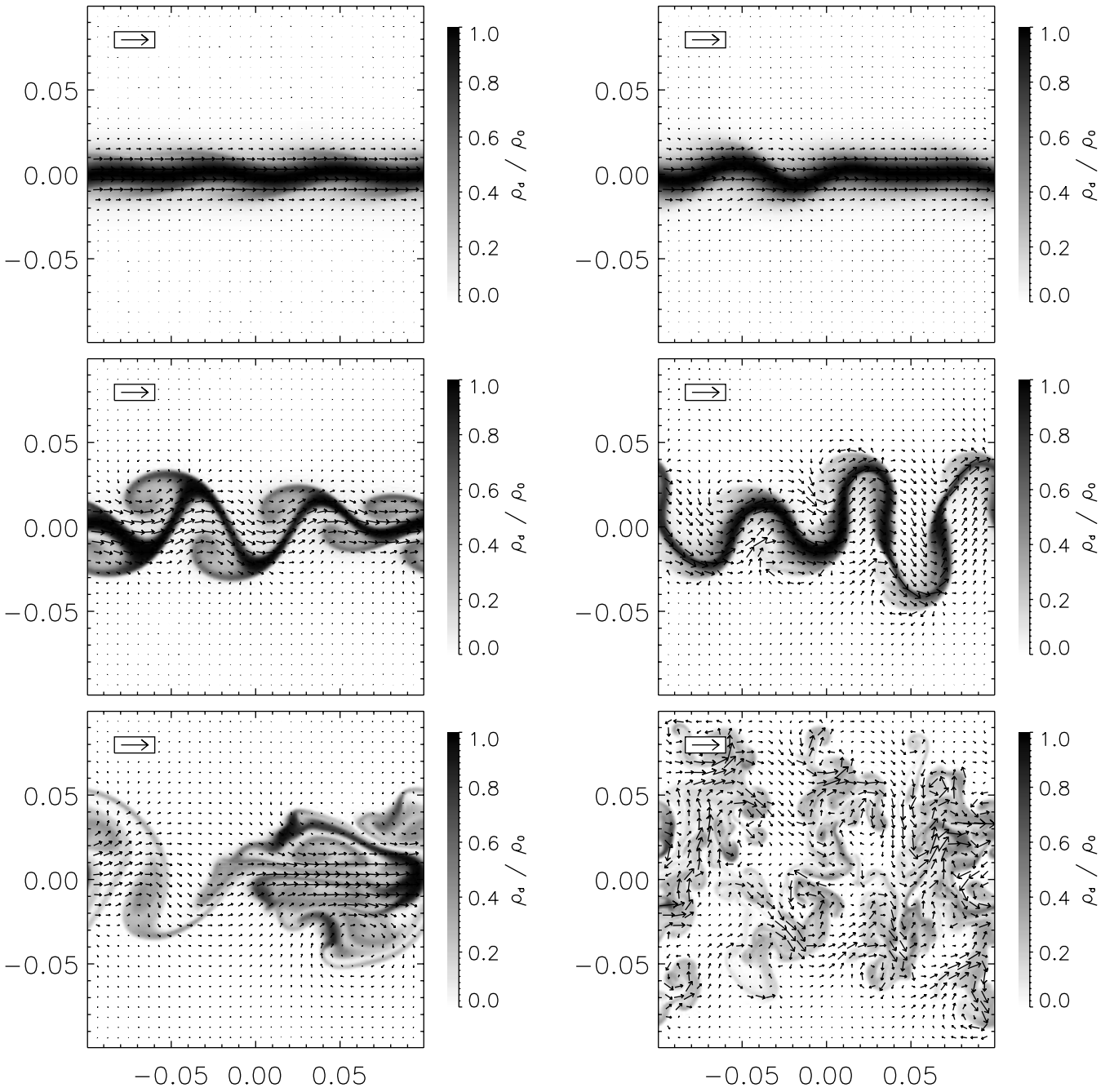

FIG. 5.—Sample snapshots from a simulation with prescribed $\mu(z)$, both with Coriolis terms turned off ($\Omega_F = 0$, *left*) and turned on ($\Omega_F \neq 0$, *right*). The gray scale shows dust density, and the arrows show the velocity in the dust-free reference frame; the arrow in the box represents a magnitude of $v_{0,\max}/c_s$. Coordinate axes are in units of H_g. Both models have $H_d = 0.01H_g$, $\Sigma_d = 0.008\Sigma_g$, and $v_{0,\max} = 0.1c_s$. Snapshots correspond to $t = (1.5, 2.2, 2.9)t_{\rm orb}$ for the left column and $t = (1.8, 2.3, 2.8)t_{\rm orb}$ for the right column.

versus $0.05\Omega_{\rm K}$. (The procedure to measure these growth rates is described in § 4.3.)

In addition to the sample cases shown, we have performed a large number of similar models with both $\Omega_F = 0$ and $\Omega_F \neq 0$ and either full or "half" grids. We have covered a range $H_d/H_g = 0.001-0.08$, with a constant surface density ratio $\Sigma_d/\Sigma_g = 0.008$. Overall, we find a confirmation of the above results: the layer evolves more rapidly when $\Omega_F \neq 0$ and more slowly when we force the development of the odd mode. We also found that for $\Omega_F = 0$ and this Σ_d/Σ_g value, the layer becomes stable for $H_d/H_g \gtrsim 0.02$. When $\Omega_F \neq 0$, the layer appeared to be always unstable, although the evolution times are quite small for the thickest layers.

4.3. *Experiments with* Ri = *constant*

The initialization procedure adopted in § 4.2 is quite simple but also quite arbitrary in terms of the detailed functional form of the dust distribution. As an alternative approach, we can adopt a prescription for the initial conditions that satisfies additional physically motivated constraints. A natural choice is to set Ri to a constant value everywhere in the flow; this choice is motivated by the common conception that low-Ri flows are unstable and

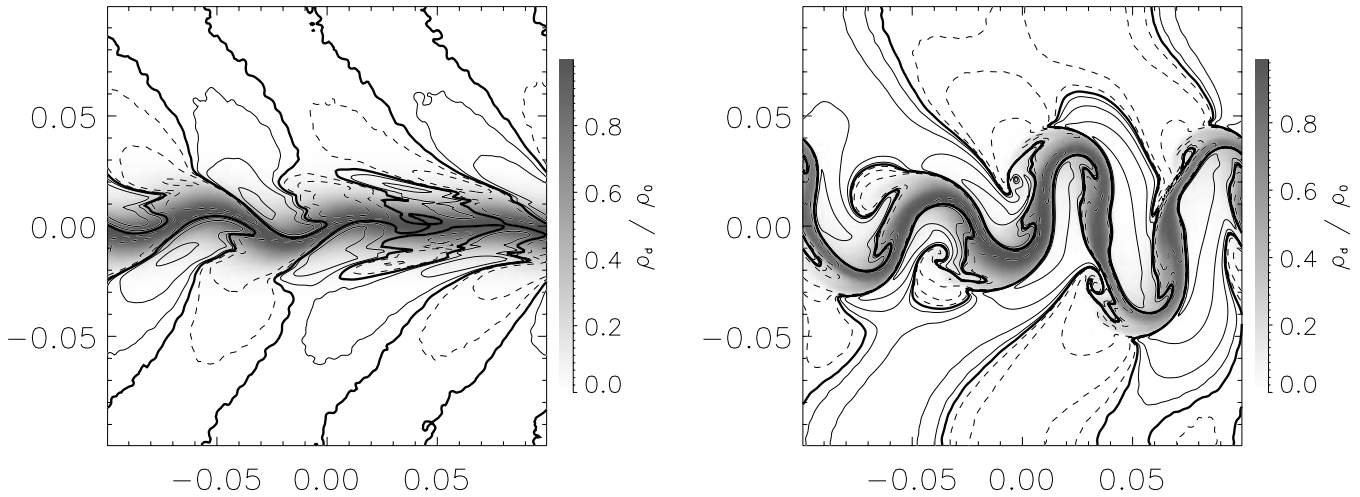

FIG. 6.—Snapshots from the $\Omega_F \neq 0$ simulation shown in Fig. 5, at $t = 1.8t_{\rm orb}$ (*left*) and $2.3t_{\rm orb}$ (*right*). The gray scale shows dust density, and lines show contours of v_x: *thin solid*, $v_x > 0$; *thick solid*, $v_x = 0$; and *dashed*, $v_x < 0$. As the perturbation grows, the dust layer experiences the slower moving high-latitude gas as a headwind. This gas steals angular momentum from the dust layer, which flows radially inward, while the dust-poor gas flows outward.

high-Ri flows are stable. In particular, Sekiya (1998) and Youdin & Shu (2002) have argued that the disk may evolve to a state in which $\mathrm{Ri} = \frac{1}{4}$ (see § 1).

Using the definition of the Richardson number in equation (1), and equations (10) and (15), we can obtain a differential equation for μ (for a given constant Ri):

$$\frac{d\mu}{dz} = \frac{-z(1+\mu)^3}{2\mathrm{Ri}H_g^2(v_{0,\max}/c_s)^2}\left[1+\sqrt{1+\frac{4\mathrm{Ri}(v_{0,\max}/c_s)^2}{1+\mu}}\right]. \quad (40)$$

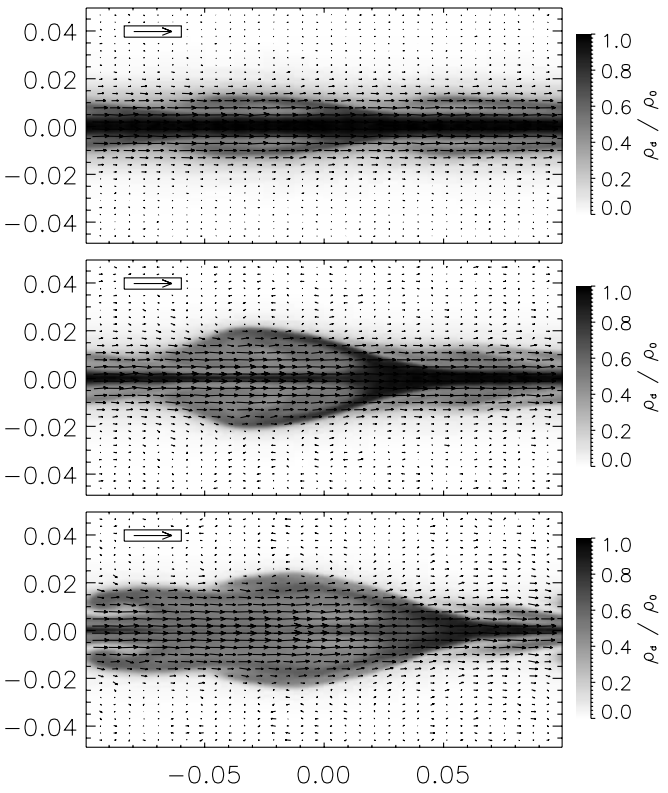

FIG. 7.—Simulation with prescribed $\mu(z)$ for the $\Omega_F = 0$ case, forcing the odd mode of the instability by placing a reflecting boundary at $z = 0$. From top to bottom, snapshots show dust density (*gray scale*) and velocity field (*vectors*) at $t = (2.5, 5.0, 7.5)t_{\rm orb}$. Notice the smaller vertical extension of the grid, compared with Fig. 5.

An approximate solution to this equation can be found provided that $4\mathrm{Ri}(v_{0,\max}/c_s)^2/(1+\mu) \ll 1$ (true for the parameter space of interest). Using this approximation,

$$1+\mu(z) = \left[\left(\frac{1}{1+\mu_0}\right)^2 + \frac{(z/H_g)^2}{\mathrm{Ri}(v_{0,\max}/c_s)^2}\right]^{-1/2}. \quad (41)$$

Again, three parameters define a model: μ_0 (or alternatively, Σ_d/Σ_g), $v_{0,\max}/c_s$, and Ri. This equation sets a finite extension for the dust layer. Setting $\mu(z) = 0$, we obtain

$$\frac{z_{\max}}{H_g} = \left\{\mathrm{Ri}\left[\frac{v_{0,\max}}{c_s}\right]^2\left[1-\frac{1}{(1+\mu_0)^2}\right]\right\}^{1/2}. \quad (42)$$

We use this setup to study the stability of the dust layer under varying conditions. Cases with and without the Coriolis terms were performed. For our array of simulations, we adopt $v_{0,\max}/c_s = 0.1$ and explore a range of initial values of Σ_d/Σ_g and Ri. Our parameter grid covered $\Sigma_d/\Sigma_g = 0.006$–$0.178$, and $\mathrm{Ri} = 0.1$–1.0 for the $\Omega_F = 0$ cases and $\mathrm{Ri} = 1.0$–10.0 for the $\Omega_F \neq 0$ cases. The domain of these simulations extended $\pm 10z_{\max}$ in y and $\pm 2z_{\max}$ in z. (We did not need a large z-extension, since these experiments were designed to follow only the linear part of the instability, as opposed to the full evolution of § 4.2.) Our standard resolution was 200×40 grid points, with higher resolution models tested for selected cases in order to verify the results. Each simulation was followed through $t/t_{\rm orb} = 400z_{\max}/H_g$, which corresponds to values between $9t_{\rm orb}$ and $40t_{\rm orb}$ for Ri between 0.1 and 1.0. The initial equilibrium setup was perturbed with random velocities with a maximum amplitude of $10^{-3}c_s$.

After exploring several possibilities, we found that a practical way of assessing the stability of the dust layer was by calculating the Fourier transform of v_z along the y-direction, as a function of z. When the layer is unstable, the fastest growing mode is easily identified from this plot; its amplitude can then be examined as a function of time. In most cases, the linear growth phase of the instability is clearly evident, and a growth rate can be measured. An example is presented in Figure 8.

As expected, the empirically determined region of stability in the parameter space does not have a sharp edge, but instead

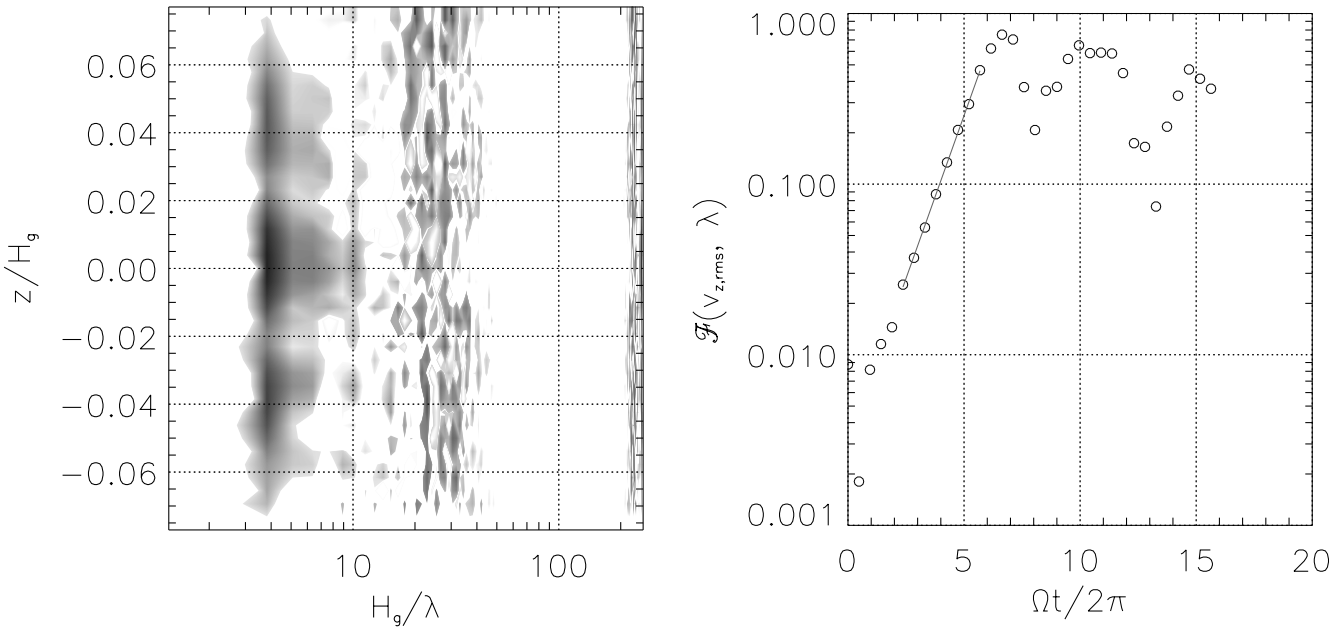

FIG. 8.—*Left*: Fourier transform of v_z along the y-direction, as a function of z, for the Ri $= 0.158$, $\Sigma_d/\Sigma_g = 0.056$, and $\Omega_F = 0$ case, after 4.27 orbital times. *Right*: Amplitude of the $\lambda = 0.26H_g$ mode, in arbitrary units, as a function of time, for $z = 0$. The linear growth phase of the instability (*solid line*) shows a growth rate $\omega_I = 0.14\Omega_K$.

growth rates decrease until our procedure becomes too insensitive to measure them. For practical purposes, we denote as "stable" those simulations that do not show growth within the allotted run time or else for which the measured growth rate is lower than a fiducial value, set to $\omega_I = 0.05\Omega_K$; this growth rate corresponds to a 10-fold increase in amplitude over 10 orbital times.

In Figure 9 we present results for an array of values in the Σ_d/Σ_g-Ri parameter space, noting whether each model is stable (S) or unstable (U) according to the above criteria. Generally speaking, the $\Omega_F = 0$ case shows stability for Ri > 0.3 (Fig. 9*a*). As in § 4.2, we also forced the development of the odd mode of the instability by placing a reflecting boundary at $z = 0$. For the odd modes, the edge of stability also appears consistent with the criterion Ri $= \frac{1}{4}$, although the measured growth rates are much lower than for the even mode.

The main difference between the $\Omega_F = 0$ and $\Omega_F \neq 0$ cases (Fig. 9*b*) is that stability in the $\Omega_F \neq 0$ case requires a much

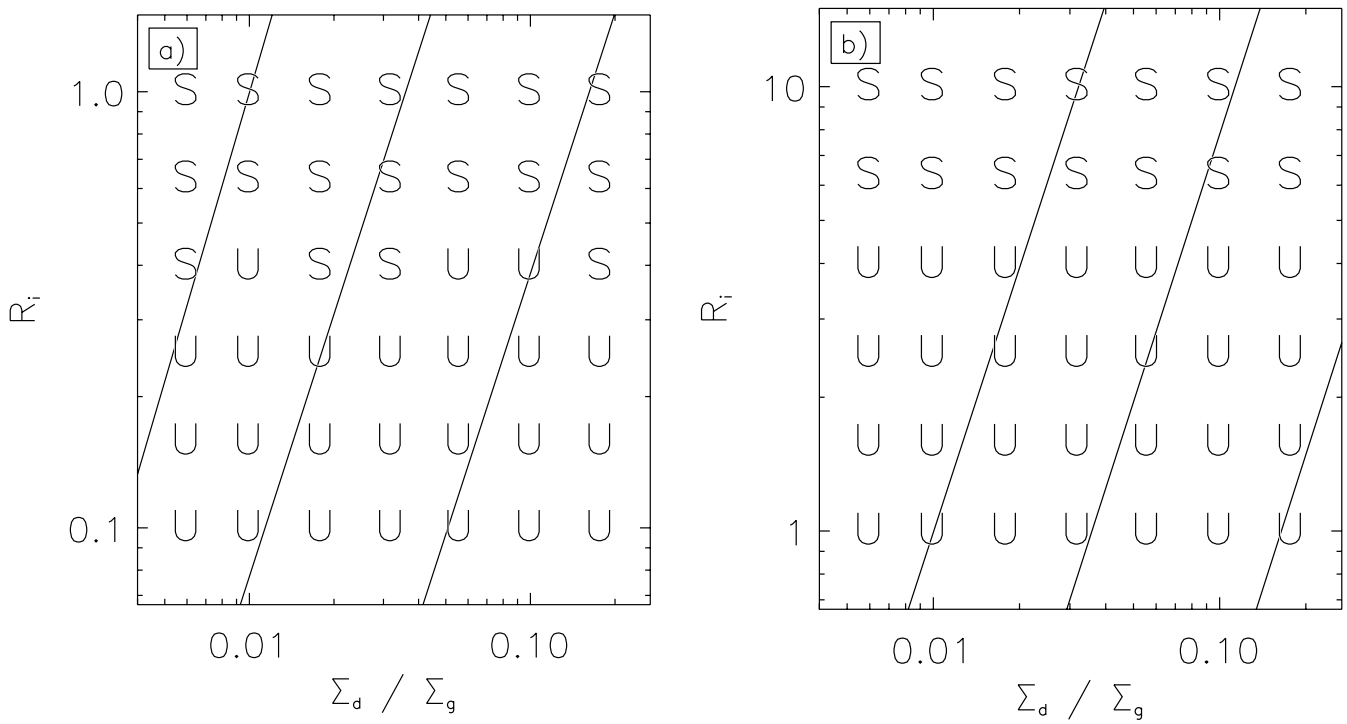

FIG. 9.—Stability in the dust layer for a matrix of values of the dust surface density Σ_d/Σ_g and Richardson number values Ri, with (*a*) Coriolis terms turned off ($\Omega_F = 0$) and (*b*) Coriolis terms turned on ($\Omega_F \neq 0$). Stable cases, based on simulation growth rates, are marked with an "S" and unstable cases with a "U." Models with a measured growth rate $\omega_I < 0.05\Omega_K$ are considered stable. The lines across these plots trace the value of the midplane dust fraction, (*from the left*) $\mu = 0.3$, 1.0, and 10. Note the different ranges of Ri in (*a*) and (*b*).

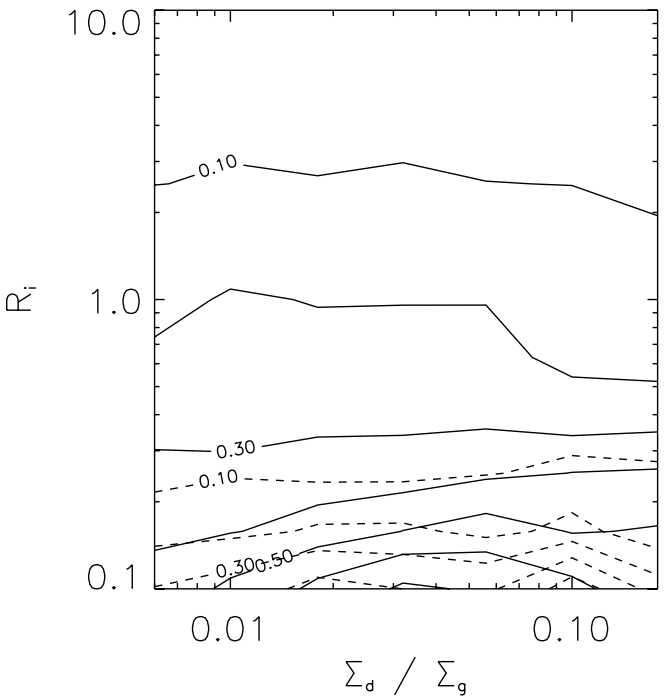

FIG. 10.—Comparison of growth rates for the $\Omega_F = 0$ (*dashed lines*) and $\Omega_F \neq 0$ (*solid lines*) cases, in units of Ω_K. The growth rates are generally higher when Coriolis terms are turned on.

larger value of the Richardson number, near Ri ~ 5. It is important to stress that this threshold value for Ri depends on the value chosen for the fiducial minimum "unstable" growth rate, since there is some subjectivity in the procedure to measure growth rates and the slope of ω_I as function of Ri is quite shallow when $\Omega_F \neq 0$ (see Fig. 10). Nevertheless, the layer is quite clearly unstable for values of Ri significantly larger than $\frac{1}{4}$. Since Ri can be thought as a proxy for the layer thickness (eq. [42]), the condition that a larger Ri is required for stability when $\Omega_F \neq 0$ is consistent with the results of § 4.2, in which we found that the final dust distribution is thicker when the Coriolis terms are turned on.

As a coda for this section, we comment on the constant-Ri distribution adopted here. Sekiya (1998) studied the profile determined by a constant-Ri dust distribution and noticed that the space density develops an infinite cusp if the Σ_d/Σ_g value is large enough. Youdin & Shu (2002) interpreted this result as a hint that the gas distribution can only sustain the weight of a mass of dust similar to its own mass and that if surpassed, the dust would precipitate. By numerically integrating our equation (41) for a given Ri = constant, together with the hydrostatic equilibrium condition in equation (15), we find that

$$\mu_0 = \frac{e}{2} \exp\left[\sqrt{\frac{\pi}{2}} \frac{\Sigma_d}{\Sigma_g} \frac{1}{\mathrm{Ri}^{1/2} v_{0,\max}/c_s}\right] \tag{43}$$

for $\mu_0 \gg 1$ (see also eq. [22] in Sekiya 1998). This means that for $\mathrm{Ri}_{\mathrm{crit}}$ of order unity, $\Sigma_d/\Sigma_g > v_{0,\max}/c_s$ implies an exponential growth of the midplane dust abundance. The onset of a cusp in density would therefore occur (under the condition Ri = constant), for a range of radii $\sim$1–10 AU (see eq. [14]), when Σ_d/Σ_g exceeds $\sim$0.1, i.e., for roughly an order-of-magnitude dust enhancement. However, this conclusion appears to be an artifact of the Ri = constant condition. If Ri is permitted to vary with height, with Ri becoming large near the midplane, then μ_0 varies only linearly rather than exponentially with Σ_d/Σ_g, and a cusp need not form.

5. SUMMARY AND CONCLUSIONS

In this work, we have studied the stability of gaseous disks with vertically varying dust abundances and accompanying vertical velocity gradients. We present both a linear analysis of a simple discrete three-layer distribution and full numerical simulations of a pair of continuous distributions. We focus on identifying and comparing criteria for instability when the Coriolis force terms are considered ($\Omega_F \neq 0$) or disregarded ($\Omega_F = 0$). Our results indicate that the Richardson number Ri is still a good general discriminant for the stability/instability boundary when $\Omega_F \neq 0$, but the critical value is larger than the classical result Ri = $\frac{1}{4}$ for $\Omega_F = 0$.

As with the well-known two-layer problem, the critical Ri for the discrete three-layer distribution depends on the wavelength of interest. We argue that wavelengths of order a few times the layer thickness ($k_y H_d \approx 1$) are the most relevant, since smaller wavelengths will yield less dust mixing in the nonlinear regime and larger ones will have smaller growth rates. In addition, for realistic vertical distributions with continuous variations of $v_y(z)$ and $\mu(z)$, waves with $k_y H_d \gg 1$ would not be unstable. For $k_y H_d = \pi/3$, $\mathrm{Ri}_{\mathrm{eff}} < 1.1$ is a necessary (but not sufficient) condition for instability for the $\Omega_F \neq 0$ case. In general, when $\Omega_F \neq 0$, marginally unstable modes first appear when $\mathrm{Ri}_{\mathrm{eff}}$ drops below $(k_y H_d)^2$. Since $\mathrm{Ri}_{\mathrm{eff}}$ is a proxy for the layer thickness, this means that when Coriolis forces are considered, the dust layer is thicker than in the $\Omega_F = 0$ case at the onset of instability. At $\Sigma_d/\Sigma_g = 0.01$, the increase in thickness is $\sim$50%, whereas for $\Sigma_d/\Sigma_g = 0.1$, the increase is nearly a factor of 3. For the $v_{0,\max}/c_s = 0.1$ value adopted throughout this work, $R = 3.5$ AU (for MSN parameters), and GI will set in only when $\mu > 187$ (Sekiya 1998). The thicker layer at the "edge" of KHI implies that the dust-to-gas surface density ratio necessary for GI (neglecting vertical self-gravity) would increase from the already high value of $\Sigma_d/\Sigma_g = 1.1$ (eq. [25]) to $\Sigma_d/\Sigma_g = 15$ (eq. [34]), when Coriolis effects are included.[5] While we certainly do not believe that our results (assuming full coupling) can be accurately extrapolated into the dust-dominated regime, this comparison gives a sense of the strong change that can be expected. The astronomical implication is, of course, that GI is even more difficult to achieve than previously thought.

We note that consideration of even-symmetry (in v_z, i.e., midplane crossing) modes is important for this problem, although some previous analytic studies (Ishitsu & Sekiya 2002, 2003, for example) have focused only on odd-symmetry modes. The even-symmetry case becomes unstable at a larger value of $\mathrm{Ri}_{\mathrm{eff}}$ than the odd-symmetry case (which is similar to the two-layer system analyzed by Chandrasekhar [1981]).

The results from our simulations are consistent with the main conclusions drawn from the simple three-layer stability analysis. Based on an array of simulations that were initialized with Ri = constant vertically, we found that Ri ~ 5 is the critical value found for the $\Omega_F \neq 0$ case. This critical Ri value should be considered an approximate result, since the procedure used to evaluate stability from the simulations involves a certain level of subjectivity. Nevertheless, the dust layer is clearly unstable for Ri values significantly larger than $\frac{1}{4}$. As with the discrete case, the

[5] For the continuous dust distribution studied by Garaud & Lin (2004), the surface density needed for GI, with these parameters and neglecting Coriolis forces, would be $\Sigma_d/\Sigma_g \approx 0.4$, only slightly lower than the value 1.1 for our three-layer model with $\Omega_F = 0$.

larger Ri value also implies a thicker dust layer; for $\Sigma_d/\Sigma_g = 0.01$ at the threshold of instability for $\Omega_F \neq 0$, the height containing half the dust surface density increases by a factor of $\sim$3 compared to the corresponding nonrotating model. Of course, both this and other results based on the strong-coupling assumption should be considered carefully when $\mu \gg 1$, i.e., for large Σ_d/Σ_g.

Youdin & Shu (2002) point out that precipitation of solids is likely to occur in layers for which $\mu \gg 1$. For vertical profiles with Ri = constant, this situation arises first at the midplane, where a density cusp forms for Σ_d/Σ_g exceeding some critical value (of order $v_{0,\max}/c_s$). They therefore conclude that, for GI to develop, Σ_d/Σ_g needs to be increased from the MSN value by a smaller amount than from estimates without a density cusp. Since our results imply that stability fails at larger Ri (and hence a thicker dust layer) than the value assumed by Youdin & Shu (2002), the total dust enhancement Σ_d/Σ_g required before a cusp is predicted (and precipitation develops) would nominally be larger than they concluded. However, it is not clear that the condition for cusp formation can in fact be obtained and written in a simple way in terms of Σ_d/Σ_g, for the reason we now discuss.

States that have Ri = constant have been considered of particular interest because they are everywhere at a nominal threshold for instability. However, the proposal that profiles should evolve to such states implicitly depends on an assumption that the localized failure of the KH stability criterion would lead to localized turbulence. While we chose a constant-Ri setup in the models of § 4.3 to facilitate comparison with previous work, the results of the simulations in fact call this implicit assumption into question. When exploring Ri(z) for the simulations in § 4.2, in some of our models the Ri $> \frac{1}{4}$ stability condition failed only for $|z| < 2H_d$. Nevertheless, the fastest growing mode in these models had $\lambda \approx 7H_d$, and the nonlinear evolution involved the whole layer, yielding dust mixing at heights over 10 times the initial H_d value. Furthermore, when the simulations were followed until the dust distribution was somewhat homogeneous in the azimuthal direction, the vertical profile did not appear to have a constant Ri value.

It is our view that as exemplified by these models, a local failure to satisfy a stability criterion that is stated in terms of local quantities need not trigger only local instabilities, i.e., of wavelengths similar to the thickness of the "failing" region. Instead, the wavelength will be similar to the overall velocity gradient, and the height of the waves when they break will be similar to the wavelength. The readjustment of the dust distribution that is generated will thus be *global*, including regions that initially have Ri $>$ Ri$_{\rm crit}$. It is, therefore, not obvious that the "final," or quasi-equilibrium, distribution should be accurately described by a local quantity. It may be that the marginal state that develops as a result of the competition between dust settling and shear-driven turbulence, in fact, has a relatively uniform distribution of dust in a central layer, rather than a cusp out of which solids can precipitate. Of course, if particles grow large enough prior to the onset of global dust-layer turbulence, then they may continue to settle faster than the growth rate of the instabilities. Since particle growth depends on uncertain sticking efficiency, however, this question remains open. Observations with newly deployed infrared telescopes should shed some light on the true vertical distribution of solids in protoplanetary disks.

For the technical modeling in this work, we have adopted a number of simplifications and idealizations. While we believe that our main conclusions are not sensitive to these assumptions, it is appropriate to review what they are. One such simplification is that we consider only models with $k_x = 0$ and neglect radial shear and tidal forces. We focused on $k_x = 0$ because these modes typically have the fastest growth rates and largest instability thresholds in terms of Ri. Had we included shear, then k_x would have grown in time as $dk_x/dt = (3/2)\Omega_{\rm K} k_y$, which would ultimately limit growth of perturbations of a given k_y. In future work, it will be important to examine how, for example, the total amplification of shearing KH wavelets depends on Ri.

Other idealizations include neglecting the slip of gas relative to dust, treating the large-scale radial gradient of pressure as fixed in time, and neglecting other sources of turbulence. Gas-dust slip can itself lead to streaming instabilities (Youdin & Goodman 2005). However, either with or without full coupling of the gas and dust, the instabilities that develop depend on the gas having consistent sub-Keplerian azimuthal velocities. This relies on having a consistent radial pressure gradient; in principle, this condition could be invalidated if there are sufficient pressure perturbations induced by turbulence or large-scale waves in the disk. The ratio of such terms, $\sim(\delta P)R/(P_0\lambda)$, could be significant even for moderate-amplitude perturbations with $\lambda \sim H_g$. In future work, we intend to explore these and other dynamical processes that may affect the settling and mixing of solids in dusty disks.

We gratefully acknowledge stimulating discussions with Jim Stone, Jeremy Goodman, and Marco Martos and helpful comments on the manuscript by Andrew Youdin, Jeremy Goodman, and an anonymous referee. The simulations presented in this paper were carried out using the Beowulf cluster administered by the Center for Theory and Computation of the Department of Astronomy at the University of Maryland. Financial support was provided by NASA grant NAG5-11767.

APPENDIX

SOLUTION TO THE DISPERSION RELATION, FOR $\Omega_F \neq 0$

The dispersion relation for the even-symmetry mode, equation (23), in the long-wavelength regime, is given in equation (32). To investigate the nature of the solutions of this nonalgebraic equation, we follow a graphical procedure similar to that in Chandrasekhar (1981, p. 498). We define

$$\xi \equiv \frac{\omega}{\Omega_{\rm K}}, \tag{A1}$$

$$\eta \equiv \frac{\omega - k_y V}{\Omega_{\rm K}} = \frac{\omega}{\Omega_{\rm K}} - \frac{\mu}{1+\mu}\frac{H_g}{H_d}\frac{v_{0,\max}}{c_s} k_y H_d, \tag{A2}$$

$$\beta \equiv \frac{2\Omega_F}{\Omega_{\rm K}}. \tag{A3}$$

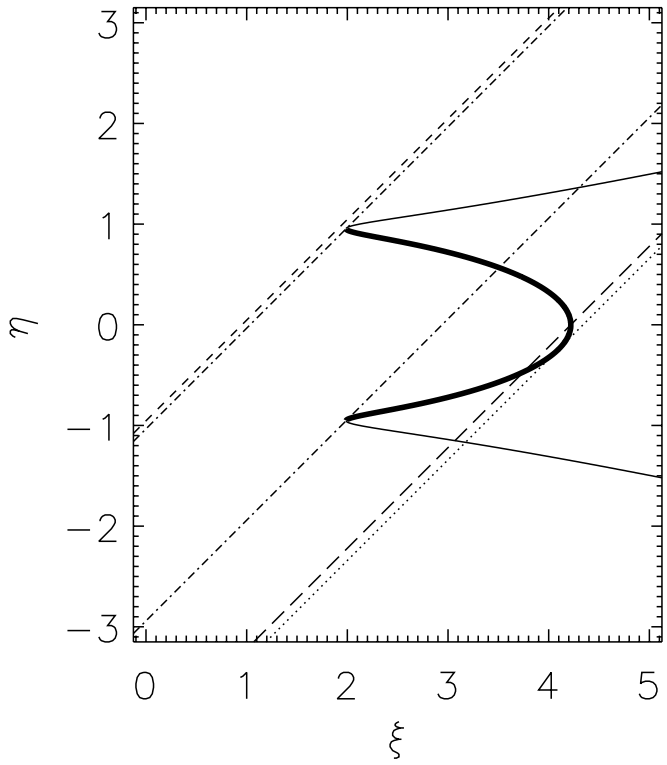

FIG. 11.—Locus of the real solutions to eqs. (A4) (*thick solid line*) and (A5) (*thin solid line*), for $k_y H_d = \pi/3$ and $\mu = 10$. Straight lines $\xi - \eta =$ constant are related to critical points of the problem (see text). For given values of $k_y H_d$, μ, and $v_{0,\max}/c_s$, varying values of $\xi - \eta$ correspond to different values for H_d/H_g.

In these variables, the dispersion relation reads

$$\eta^2 = \frac{\mu}{1+\mu}\left[1 - \frac{\xi^2}{\mu k_y H_d}\left(1 - \frac{\beta^2}{\xi^2}\right)^{1/2}\right]. \tag{A4}$$

By simultaneously considering the equation

$$\eta^2 = \frac{\mu}{1+\mu}\left[1 + \frac{\xi^2}{\mu k_y H_d}\left(1 - \frac{\beta^2}{\xi^2}\right)^{1/2}\right], \tag{A5}$$

together with the relation $|\xi - \eta| = k_y V/\Omega_K =$ constant, we can obtain a fourth-order polynomial instead of a nonalgebraic equation. All the solutions of the polynomial must be solutions either of equation (A4) or (A5).

The thick solid line in Figure 11 shows the locus of the real solutions of equation (A4), which we shall call the *P*-branch, while the thin solid lines show the real solutions of equation (A5), which we shall call the *S*-branch. For clarity, we show only the $\xi > 0$ side of the diagram. In addition, Figure 11 shows several lines representing $|\xi - \eta| =$ constant, which relate to a series of critical points (ξ, η) for the problem as follows:

1. The ends of the *P*-branch lie at $(\pm\beta, \pm\eta_0)$; these are the intersections with the dash-dotted lines $\xi - \eta = \beta \pm \eta_0$ in Figure 11. Here $\eta_0^2 = \mu/(1+\mu)$.
2. The maximum extension of $|\xi|$ for the *P*-branch lies at $(\pm\xi_0, 0)$; this is the intersection with the long-dashed line $\xi - \eta = \xi_0$ in Figure 11. Here $\xi_0^2 = [(\mu k_y H_d)^2 + \beta^4/4]^{1/2} + \beta^2/2$.
3. The point of the *P*-branch with the maximum value of $|\xi - \eta|$, (ξ_t, η_t); this is at the intersection with the dotted line in Figure 11.
4. The $(\xi, \eta) = (0, -\eta_0)$ point, where $\eta_0^2 = \mu/(1+\mu)$; the short-dashed line $\xi - \eta = -\eta_0$ in Figure 11 runs through this point.

Any of the four solutions to the equivalent fourth-order polynomial must be a solution of either equation (A4) or (A5), and the number or nature of the roots of each equation can change only at the critical points outlined above. The roots corresponding to equation (A4) are shown in Figure 4, for an array of H_d/H_g (or equivalently $|\xi - \eta|$) values, given $\mu = 1$ (Fig. 4*a*), and $\mu = 10$ (Fig. 4*b*), and $k_y H_d = \pi/3$.

On the left the diagrams in Figure 4, at small H_d/H_g (or on the right of Fig. 11, at large $|\xi - \eta|$), there is a pair of complex roots. In Figure 4*b*, these two complex roots become real as $|\xi - \eta|$ becomes less than $\xi_t - \eta_t$, since then a $|\xi - \eta| =$ constant line crosses the *P*- and *S*-branches four times, implying all four roots are real. Moving farther right in Figure 4*b* (or left in Fig. 11), one of those roots becomes complex when $|\xi - \eta| < \beta + \eta_0$, and the other real root disappears when $|\xi - \eta| < \beta - \eta_0$. In Figure 4*a*, at lower μ, a complex root is present whenever a real root exists. At the far right in Figures 4*a* and 4*b* (corresponding to the region of Fig. 11 with $|\xi - \eta| < \eta_0$), there are no solutions.

There is a range of values of $|\xi - \eta|$ with all real solutions (implying stability for that set of parameters) if the *P*-branch has a section with $|d\eta/d\xi| < 1$. When that happens (as for the $\mu = 10$ case of Fig. 4*b*), the points of the *P*-branch with $|d\eta/d\xi| = 1$ lie very close to the $(\beta, -\eta_0)$ and $(\xi_0, 0)$ points. So, a good approximation for the opening of such a stability gap is $\xi_0 > \beta + \eta_0$. While it is straightforward to find a precise criterion for the existence of this gap, it is of limited practical significance since the gap closes for longer wavelengths (which yield more efficient vertical mixing). We consider more significant the fact that there are no solutions, real or complex, for $|\xi - \eta| < \eta_0$, since this yields a necessary (but not sufficient) condition for instability.

REFERENCES

Champney, J. M., Dobrovolskis, A. R., & Cuzzi, J. N. 1995, Phys. Fluids, 7, 1703
Chandrasekhar, S. 1981, Hydrodynamic and Hydromagnetic Stability (New York: Dover)
Coradini, A., Federico, C., & Magni, G. 1981, A&A, 98, 173
Cuzzi, J. N., Dobrovolskis, A. R., & Champney, J. M. 1993, Icarus, 106, 102
Cuzzi, J. N., Dobrovolskis, A. R., & Hogan, R. C. 1994, Lunar Planet. Sci. Conf., 25, 307
Drazin, P. G., & Reid, W. H. 1981, Hydrodynamic Stability (Cambridge: Cambridge Univ. Press)
Garaud, P., & Lin, D. N. C. 2004, ApJ, 608, 1050
Goldreich, P., & Ward, W. R. 1973, ApJ, 183, 1051
Haghighipour, N., & Boss, A. P. 2003, ApJ, 583, 996
Hayashi, C. 1981, Prog. Theor. Phys. Suppl., 70, 35
Howard, L. N. 1961, J. Fluid Mech., 10, 509
Huppert, H. E. 1968, J. Fluid Mech., 33, 353
Ishitsu, N., & Sekiya, M. 2002, Earth Planets Space, 54, 917
———. 2003, Icarus, 165, 181
Li, L.-X., Goodman, J., & Narayan, R. 2003, ApJ, 593, 980
Miles, J. W. 1961, J. Fluid Mech., 10, 496
Nakagawa, Y., Nakasawa, K., & Hayashi, C. 1981, Icarus, 45, 517
Nakagawa, Y., Sekiya, M., & Hayashi, C. 1986, Icarus, 67, 375
Rice, W. K. M., Lodato, G., Pringle, J. E., Armitage, P. J., & Bonnell, I. A. 2004, MNRAS, 355, 543
Safranov, V. S. 1969, Evolution of the Protoplanetary Cloud and the Formation of the Earth and Planets (Moscow: Nauka Press)
Sekiya, M. 1983, Prog. Theor. Phys., 69, 1116
———. 1998, Icarus, 133, 298
Sekiya, M., & Ishitsu, N. 2000, Earth Planets Space, 52, 517
———. 2001, Earth Planets Space, 53, 761
Stone, J. M., & Norman, M. L. 1992, ApJS, 80, 753
Tanga, P., Weidenschilling, S. J., Michel, P., & Richardson, D. C. 2004, A&A, 427, 1105
Weidenschilling, S. J. 1977, MNRAS, 180, 57
———. 1980, Icarus, 44, 172
———. 1995, Icarus, 116, 433
———. 2003, Icarus, 165, 438
Weidenschilling, S. J., & Cuzzi, J. N. 1993, in Protostars and Planets III, ed. E. H. Levy & J. I. Lunine (Tucson: Univ. Arizona Press), 1031
Youdin, A. N., & Chiang, E. I. 2004, ApJ, 601, 1109
Youdin, A. N., & Goodman, J. 2005, ApJ, 620, 459
Youdin, A. N., & Shu, F. H. 2002, ApJ, 580, 494